

pubs.acs.org/acscatalysis Research Article

# Parallelized Screening of Characterized and DFT-Modeled Bimetallic Colloidal Cocatalysts for Photocatalytic Hydrogen Evolution

Eric M. Lopato, Emily A. Eikey, Zoe C. Simon, Seoin Back, Kevin Tran, Jacqueline Lewis, Jakub F. Kowalewski, Sadegh Yazdi, John R. Kitchin, Zachary W. Ulissi, Jill E. Millstone, and Stefan Bernhard\*



Cite This: ACS Catal. 2020, 10, 4244-4252



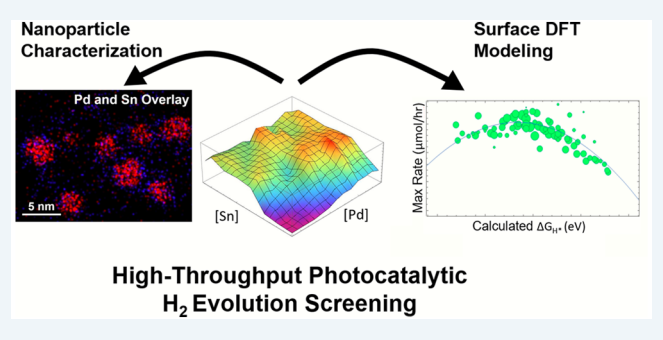
**ACCESS** 

Metrics & More

Article Recommendations

Supporting Information

ABSTRACT: Using a newly designed and developed parallelized photoreactor and colorimetric detection method, a large sampling of bimetallic cocatalysts (Pd/Sn, Pd/Mo, Pd/Ru, Pd/Pb, Pd/Ni, Ni/Sn, Mo/Sn, and Pt/Sn) for photocatalytic water reduction have been tested. Of these cocatalysts, the combination of palladium and tin showed the highest synergistic behavior and peak hydrogen gas production at a low relative fraction of palladium. The resulting palladium/tin bimetallic cocatalysts were characterized, and specifically, and scanning transmission electron microscopy energy-dispersive X-ray spectroscopy indicated that palladium and tin elements reside within the same particle. The experimental



catalytic activity for the palladium/tin mixture was compared to density functional theory-derived energy values associated with the adsorption of hydrogen onto a surface. This comparison demonstrated that the typical peak found in electrochemical Sabatier volcano plots at  $\Delta G_{H^*} = \sim 0$  eV were replicated in the experimental photocatalytic system with a peak activity observed at  $\Delta G_{H^*} = -0.036$  eV. Computational confirmation of the results expressed here demonstrates the efficacy of colorimetric detection of hydrogen in parallel and presents a model for increasingly rapid catalyst screening.

KEYWORDS: parallel, photocatalytic, nanoparticle, 96-well, DFT, iridium, hydrogen

#### INTRODUCTION

In order to secure a sustainable, solar-driven energy future, work is being done to ensure the readiness of alternative fuels. A variety of solar fuels provide promising alternatives for portable carriers necessary for transportation where fossil fuels still dominate. Evolution of gaseous hydrogen (H<sub>2</sub>) from water via photocatalytic water-splitting has garnered much attention in recent years.<sup>2</sup> Advantages of this method over conventional H<sub>2</sub> production through steam reforming are clear because the consumed material (water) is both highly abundant and inexpensive, and the resulting H<sub>2</sub> is light and energy-dense. However, the production of H<sub>2</sub> through photocatalytic watersplitting has long struggled to reach a level of practical efficiency. Previous work from the Bernhard Group has provided efficient water reduction systems using iridium-based photosensitizers (PSs) in combination with colloidal platinum, palladium or nickel water reduction catalysts (WRCs).<sup>3,4</sup> A more recent goal of this work was not only to identify an extraordinary solar fuel system integrating more abundant and more accessible components, but also to dive further into understanding why the catalysts are effective in an effort to aid in the discovery and translation of these catalysts into viable alternative fuel sources. Along these lines, a library of previously untested bimetallic cocatalysts was investigated for photocatalytic water reduction in this work. Although present in electrocatalytic water-splitting<sup>5,6</sup> or semiconductor studies,<sup>7,8</sup> there appears to be minimal literature on bimetallic colloidal catalysts for visible light-driven photocatalytic water reduction in a solution-based system.

Conversely, water reduction systems employing bimetallic catalysts have gathered significant attention in computational studies. <sup>9,10</sup> Following from the Sabatier principle, a variety of studies have reported catalytic volcano plots connecting the activity of electrocatalytic surfaces to hydrogen binding energies at these surfaces as calculated by density functional theory (DFT). <sup>11</sup> In testing our bimetallic systems, we calculated binding energies for a variety of compositions to determine if the electrocatalytic Sabatier principle also applies to photocatalytic systems with in situ formed nanoparticulate cocatalysts.

Received: December 13, 2019 Revised: March 5, 2020 Published: March 6, 2020



To efficiently investigate the relationship between computational and experimental studies, we have established a parallelized system intended to reduce waste and increase screening speed in solar fuels research by generating real-time data for photocatalytic reactions. These findings can be fed into any number of computational systems to determine their reliability while providing data on the kinetics and robustness of H<sub>2</sub>-forming reactions. To rapidly assess the production of H<sub>2</sub> a chemosensory tape is employed, which gives a visual, measurable analytical signal throughout the process, presenting a quantifiable measure of the H<sub>2</sub> content in the headspace above the solutions. Likely because of the lower experimental throughput of earlier studies, little work was done involving earth-abundant metal particles as a vast majority of these combinations do not provide substantial catalytic results. Palladium was chosen as a starting point due to its wellreported, robust catalytic performance in water reduction reactions. From palladium, we chose a set of metals for earth abundancy as well as proximity in the periodic table. The work focused particularly on palladium/tin due to its diverse catalytic capacity in nitrate reduction, 12 nitrate removal from drinking water, 13 hydrogen peroxide direct synthesis, 14 carbon monoxide oxidation, 15 and ethanol oxidation. 16

#### EXPERIMENTAL

**Photoreactor Design and Calibration.** Our unique photoreactor design has expanded our capacity for parallelized experimentation (Figure 1). Our system employs an aluminum

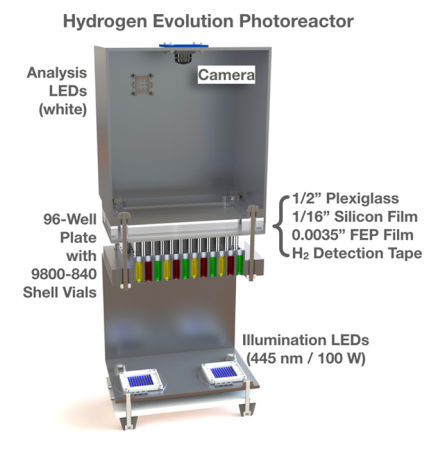
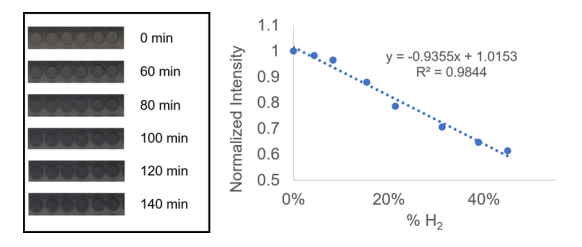


Figure 1. 3D diagram of photoreactor design.

plate machined to fit 96 1 mL shell vials. Small holes were drilled in the bottom of the reactor plate to allow illumination from the light-emitting diodes (LEDs) located directly underneath. The vials were then covered in a chemosensory colorimetric  $\rm H_2$ -sensitive tape (DetecTape Hydrogen Detection Tape—Midsun Specialty Products, Item DT-H210015-PF4) to observe and quantify  $\rm H_2$  evolution kinetics. To create a gas-impermeable seal in each vial, a film of fluorinated ethylene propylene (FEP) was placed over the DetecTape. To further ensure uniform sealing of all vials, a layer of 1/16'' silicon film was then added, and the whole system was clamped closed with clear plexiglass and an aluminum flange structure. To track the generation of  $\rm H_2$  in each well, visualized as darkening of the tape, pictures are taken from above the setup throughout the reaction.

This new colorimetric chemosensitive system was calibrated with known amounts of  $H_2$ . For this calibration experiment, DetecTape was sealed with FEP, silicon, and plexiglass, on top of

a set of shell vials with holes drilled in the bottom. Custom-made, silicon septa, with one side coated in FEP to contain the injected  $\rm H_2$ , were placed under each vial. Known amounts of atmospheric pressure of  $\rm H_2$  were then injected through these septa using a gas-tight syringe, and the vials were left for 10 min to allow enough time for an analytical response before a picture was taken. Pictures were then taken of the tape, and red-greenblue values were extracted for a diameter incorporating a set of 54 pixels in the center of each well. These values were then averaged and ratioed with the values from the first image taken prior to the addition of  $\rm H_2$ . The calibration curve shows a linear relationship between the normalized change in intensity and the  $\rm H_2$  concentration added (Figure 2). This calibration was then used to evaluate the percent  $\rm H_2$  produced in the parallel photoreactions.



**Figure 2.** (Left) Selection of six wells cropped from images obtained from a uniform water reduction plate showing the darkening of the  $H_2$ -sensitive tape by the  $H_2$  produced in the shell vial underneath. (Right) Calibration curve for the tape in the photoreactor presented as intensity normalized to intensity without added  $H_2$ . Percent  $H_2$  is shown as relative contribution of partial pressure to the total pressure present. Each point is an average of the values taken from various wells placed across the 96-well plate at a particular  $H_2$  content.

To determine the measurement error of the system, a uniform reaction mixture for water reduction was prepared in each well and illuminated to produce H<sub>2</sub>. This system consisted of 0.25 mM iridium-based PS ( $[Ir(Fmppy)_2dtbbpy]PF_{6}$ , Fmppy = 4'fluoro-2-phenyl-5-methylpyridine, dtbbpy = 4,4'-di-tert-butyl-2,2'-bipyridine),<sup>3</sup> 0.125 mM dimethyl viologen, 0.125 mM potassium tetrachloropalladate(II), and ~6% (w/w) triethanolamine (TEOA) in water, all combined in a 4:1 dimethylsulfoxide (DMSO)/water solvent mixture at 440  $\mu$ L total volume. The 96well plate demonstrated a standard error of 9.8% in the maximum H<sub>2</sub> produced and 12.3% in the maximum rate determined. This is consistent with a previous work using pressure sensing to detect the formation of H<sub>2</sub>.<sup>17</sup> Data resulting from this experiment can be found in the Supporting Information (Figures S1-S4), and a series of photographs cropped to depict six wells is shown in Figure 2.

In order to probe bimetallic cocatalysts at various metal ratios, experiments were performed by varying the concentrations of the two different metals across the rows and columns of a 96-well plate. Each reaction vial contained 400  $\mu$ L of DMSO (J.T. Baker JT9224) and 40  $\mu$ L of a 30% (w/w) aqueous TEOA (Alfa Aesar L04486) solution. Concentrations of the metal salts which formed the nanoparticulate catalysts were varied from 0 to 0.65 mM, whereas across the plate, a constant concentration of 0.25 mM [Ir(Fmppy)<sub>2</sub>dtbbpy]PF<sub>6</sub> was used as a PS. The following bimetallics were studied: Pd/Sn, Pd/Mo, Pd/Ru, Pd/Pb, Pd/Ni, Ni/Sn, Mo/Sn, and Pt/Sn. Metal-cation precursors used included: nickel(II) chloride anhydrous, Alfa Aesar B22085; potassium tetrachloroplatinate(II), Alfa Aesar 11048; ruthenium(III) chloride hydrate, Sigma-Aldrich 206229;

ACS Catalysis pubs.acs.org/acscatalysis Research Article

molybdenum(III) chloride, Beantown Chemical 132345; potassium tetrachloropalladate(II), Beantown Chemical 129355; lead(II) chloride, Sigma-Aldrich 268690; and tin(II) chloride dihydrate, Fisher Scientific S25578. Reactions were performed in a sealed vessel under atmospheric conditions while being illuminated by two water-cooled 100 W blue LEDs (Chanzon High Power Led Chip 100 W, 440–450 nm/3000 mA/DC 30–34 V) for 750 min.

Quantification of the system included the processing of images across the entire reaction time to yield useful values such as the total  $\rm H_2$  generated by the system and the maximum rate of  $\rm H_2$  generation. Maximum  $\rm H_2$  generated was determined by finding the maximum value in the timestamped list of detected  $\rm H_2$  quantity. Maximum rate of  $\rm H_2$  generation was determined by taking a four-point moving average across the  $\rm H_2$  quantity, finding a two-point derivative of this, taking a 12-point Gaussian filter to smooth the derivative, and determining the maximum value of the smoothed derivative of the  $\rm H_2$  traces. Representative images from the Pd/Sn experiment along with the resulting kinetic traces of  $\rm H_2$  evolution as determined by our computer vision processing system on a Mathematica platform (see the Supporting Information) are shown in Figure 3.

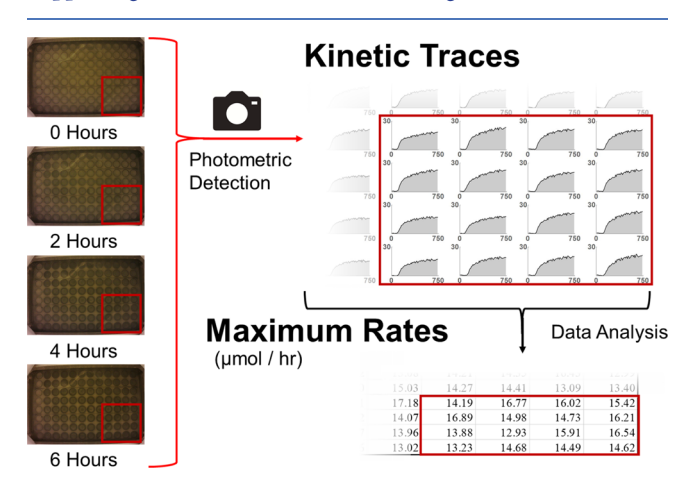


**Figure 3.** Images from the Pd/Sn bimetallic-catalyst variation test at different times through the reaction. These are processed through computer vision in Mathematica to give the kinetic traces for each well. Here, a red box surrounding 16 wells is depicted along with the resulting traces. From these traces, the maximum rate for each well can be extracted.

## Characterization of Resulting Bimetallic Catalysts.

Transmission electron microscopy (TEM) samples were prepared by drop casting an aliquot of the unwashed solution onto a carbon-backed 200 mesh Cu TEM grid (Ted Pella, Inc.), dried under ambient conditions after wicking excess solvent through the grid, and stored under vacuum prior to analysis. A Hitachi H-9500 microscope operating at 300 kV (Nanoscale Fabrication and Characterization Facility, Petersen Institute of Nanoscience and Engineering, University of Pittsburgh, PA) was used for all bright-field (BF) imaging. Images were analyzed using Digital Micrograph v2.10.1282.0 (Gatan, Inc.) and/or ImageJ v 1.47d (National Institutes of Health, USA) software. Samples for high-angle annular dark-field (HAADF) and scanning TEM energy dispersive X-ray spectroscopy (STEM-EDS) analyses were prepared by drop casting an aliquot of the washed solution (see the washing details below) onto an ultrathin carbon-backed Au TEM grid (Ted Pella, Inc.), dried under ambient conditions, and plasma cleaned for 3 s using 25%

oxygen—75% argon mix plasma prior to analysis. A probe corrected FEI Titan Themis S/TEM microscope equipped with a Super-X quad EDS detector at 300 kV (Renewable and Sustainable Energy Institute, University of Colorado at Boulder, CO) was used for the collection of HAADF images and STEM-EDS elemental maps. EDS elemental maps were collected using a FEI CompuStage high-visibility, low-background double tilt holder, and Velox software (Thermo Fisher Scientific, Inc.) was used for drift correction during acquisition and processing of data. The EDS maps were acquired using 4k channels from 0 to 20 keV with 5 eV dispersion using the Pd L $\alpha$  and Sn L $\alpha$  lines. Linescans were generated using Velox software using the Pd L $\alpha$ and Sn L $\alpha$  lines. A JEOL JEM 2100F microscope at 200 kV (Nanoscale Fabrication and Characterization Facility, Petersen Institute of Nanoscience and Engineering, University of Pittsburgh, PA) was used for the collection of linescans. Linescans were collected using a beryllium double tilt holder (JEOL #31640), and Oxford AZtec software was used for drift correction during acquisition and processing of data. The EDS linescans were acquired using 2k channels from 0 to 20 keV using the Pd L $\alpha$  and Sn L $\alpha$  lines.

Prior to HAADF and STEM–EDS analyses, the resulting bimetallic catalysts were washed. In brief, 440  $\mu$ L of the reaction solution (volume of single reaction vial) was transferred to a 1.5 mL centrifuge tube and 1 mL of ethanol (190 proof (95%), DeconTM Labs) was added. The particles were centrifuged at 20,817 rcf (Eppendorf 5424 centrifuge) for 12 min. The supernatant was removed and discarded. The pellet was resuspended in 1 mL of ethanol, and this washing process was repeated 3 more times. The final nanoparticle pellet was resuspended in 1 mL of ethanol using sonication (Fisher Scientific Ultrasonic Bath, Model 15337408) before characterization.

Prior to XPS analysis, the resulting bimetallic catalysts were washed in a similar manner to the samples prepared for TEM analysis. In brief, 440  $\mu$ L of the reaction solution (volume of single reaction vial) was transferred to a 1.5 mL centrifuge tube and 1 mL of ethanol was added. The particles were centrifuged at 20,817 rcf for 30 min. The supernatant was removed and discarded. The pellet was resuspended in minimal solvent using sonication, and a total of 12 reaction vials were washed and the resulting pellets combined. The samples were prepared by drop casting an aliquot of washed nanoparticles onto p-doped (boron) silicon wafers (University Wafer, Boston, MA) that had been cleaned for ultrahigh vacuum analysis. To remove the residual DMSO, the wafers were heated on a hot plate (Corning PC-420D) near 189 °C. XPS spectra were obtained using an ESCALAB 250XI XPS with a monochromated, microfocused Al Kα X-ray source (Materials Characterization Laboratory, Department of Chemistry, University of Pittsburgh, PA) at a spot size of 900  $\mu$ m. Survey and high-resolution spectra were collected with a pass energy of 150 and 50 eV and a step size of 1.0 and 0.1 eV, respectively. Spectra were collected after argon ion sputtering (ion energy of 4000 eV for 180 s) to remove any surface contamination. All spectra were charge referenced to adventitious carbon (284.8 eV) and fitted using Thermo Scientific Advantage software.

Computational Exploration of Pd/Sn Surfaces. We performed DFT calculations using the Vienna Ab initio Simulation Package code (version 5.4)<sup>18</sup> with the RPBE exchange—correlation functional<sup>19</sup> and projector augmented wave<sup>20</sup> pseudopotential with a kinetic energy cutoff of 350 eV. Intermetallic alloys consisting of Pd and Sn with various ratios

were collected from the Materials Projects,  $^{21}$  and all unique surfaces with Miller indices up to 2 were modeled. All MPIDs, search queries of Materials Project, studied in this work are summarized in the Supporting Information (Table S1). For each surface, we calculated single hydrogen atom (H\*) binding energies at all unique active sites. For all surface geometries, at least 20 Å of a vacuum layer was added in the *z*-direction to avoid unwanted interactions between repeating atomic structures. Convergence criteria for electronic self-consistent iteration and geometry optimization were set to  $10^{-4}$  eV and 0.03 eV/Å, respectively. For materials that have not yet been calculated due to unstable bulk structures or too many atoms in the bulk structures, we used a machine learning model to predict H\* binding energies.  $^{22}$ 

We calculated H binding energies on catalyst surfaces as follows

$$\Delta E_{H^*} = E[\text{slab} + H^*] - E[\text{slab}] - 0.5^* E[H_2] \tag{1}$$

where  $E[\operatorname{slab} + \operatorname{H*}]$ ,  $E[\operatorname{slab}]$ , and  $0.5*E[\operatorname{H}_2]$  are DFT-calculated electronic energies of H-adsorbed slab, clean slab, and  $\operatorname{H}_2$  gas molecule, respectively. The electronic binding energies were then converted into binding free energies ( $\Delta G_{\mathrm{H*}}$ ) by adding free-energy corrections for the adsorbate ( $\operatorname{H*}$ ) using a harmonic oscillator approximation at 298.15 K and for  $\operatorname{H}_2$ , using the ideal gas approximation at 298.15 K and 101,325 Pa as implemented in atomic simulation environment, <sup>23</sup> that is collectively 0.24  $\mathrm{eV}^{21}$  ( $\Delta G_{\mathrm{H*}} = \Delta E_{\mathrm{H*}} + 0.24$ ). Because adsorbed  $\mathrm{H*}$  is the only reaction intermediate in the hydrogen evolution reaction ( $\mathrm{HER}$ ),  $\Delta G_{\mathrm{H*}}$  is an effective descriptor to predict the catalytic activity of surfaces as evidenced in the literature. <sup>24</sup>  $\Delta G_{\mathrm{H*}}$  close to 0 eV indicates thermoneutral reaction energetics and thus, high HER activity.

## ■ RESULTS AND DISCUSSION

Photocatalytic water reduction systems are traditionally composed of a sacrificial donor, a PS, and a WRC. The catalytic cycle studied in this work is depicted in Figure 4. <sup>25,26</sup> In this

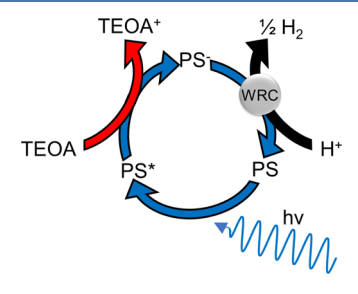


Figure 4. Photocatalytic cycle involving [Ir(Fmppy)<sub>2</sub>dtbbpy]PF<sub>6</sub> as a PS, TEOA as the sacrificial electron donor, and the nanoparticulate in situ formed bimetallic catalyst (WRC), which was varied by composition and component mixture.

work, we use [Ir(Fmppy)<sub>2</sub>(dtbbpy)]PF<sub>6</sub>, a PS that has been extensively studied for its photophysical properties and catalytic activity.<sup>27–29</sup> For the in situ formed WRC, quantifying all possible bimetallic combinations using various metal salt precursors and concentrations would lead to an insurmountable number of combinations. For this study, rather than spending time on an exhaustive search, a representative sample of metals spanning the periodic table were chosen for evaluation. A selection of metal chloride salts was used and evaluated on a range of concentrations and ratios. The reaction conditions have

been altered from previous experiments by the Bernhard Group to work under ambient atmospheric conditions rather than under argon or nitrogen.<sup>3,4,17</sup> By working in air, data can be collected rapidly under realistic water-splitting conditions without the need for a glove box or purging with inert gasses.

Screening began with Pd because it was previously shown to be a highly effective and robust catalyst in photocatalytic water reduction, 30 and combinations of Pd with metals including Sn, Ni, Pb, Mo, and Ru were subsequently explored in this work to determine if the combination of these metals with Pd would exceed the catalytic performance of Pd alone. Sn was chosen as a metalloid to test intermetallic combinations and due to the previously studied improvement of the catalytic activity in diverse Pd-catalyzed processes.  $^{12-16}$  Ni was also chosen, as it is miscible with Pd at all compositions, according to the phase diagram.<sup>31</sup> After observation of the synergistic behavior in Pd/ Sn, Pd/Pb was investigated, as Pb is expected to have similar properties to Sn. The substantially cheaper 4d cousins of Pd, Mo and Ru, were also investigated. Kinetic traces for the H2 production with WRCs formed from each metal combination and the output data for each sample can be found in the Supporting Information (Figures S1–S4, ESI file).

Values for the maximum rate of  $H_2$  evolution were measured for the bimetallic mixtures and compared to the expected values, determined by adding the activity of their component pure individual metals. The activity of individual metal samples was used as a baseline after being fit with fourth-order polynomial functions throughout the investigated concentration range, as not all metals displayed a simple linear correlation between  $H_2$  evolution activity and concentration. Specifically, Pd presents a peculiar and interestingly shaped function, as can be seen in Figure 5. At higher concentrations, Pd is less active and appears

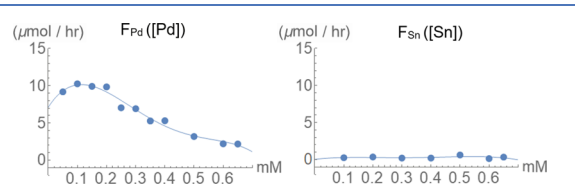


**Figure 5.** Maximum rates of single-metal catalysts at tested concentrations with fourth-order polynomial fits used to describe activity. The data for (left) Pd and (right) Sn maximum activities was used to evaluate the synergism observed in Pd/Sn bimetallic mixtures at various concentrations.

to display peak performance between 0.1 and 0.2 mM, at which range the rates outpace even those of Pt. Sn has near-zero activities over the concentration range studied (Figure 5). Fits for each other individual metal tested can be found in the Supporting Information (Figure S5).

In order to determine if the combination of metals resulted in synergistic behavior or antagonistic behavior, the combined activities for each bimetallic system were determined

Combined activity

= MaxRate(
$$[M_1]$$
,  $[M_2]$ ) -  $(F_{M_1}([M_1]) + F_{M_2}([M_2]))$ 
(2)

where MaxRate( $[M_1]$ ,  $[M_2]$ ) is the maximum rate of metal 1 and metal 2 (the bimetallic system),  $F_{M_1}([M_1])$  is the maximum rate of metal 1 only, and  $F_{M_2}([M_2])$  is the maximum rate of metal 2 only. This metric results in the differential activity of a bimetallic

WRC compared to the linear combination of the single-metal WRC activities at a particular concentration. If the combined activity was greater than zero, the combination of metals behaved synergistically. If the combined activity was negative, the combination of metals behaved antagonistically. The combined activities and metal salt concentrations associated therein can be found in the Supporting Information (Table S2). From this analysis, we can envision the capacity of a system to operate with substantially less Pd than was expected. The combined activities for each bimetallic system are plotted as a function of molar fraction of Pd or Sn over the range of concentrations investigated (Figure 6). These results demon-

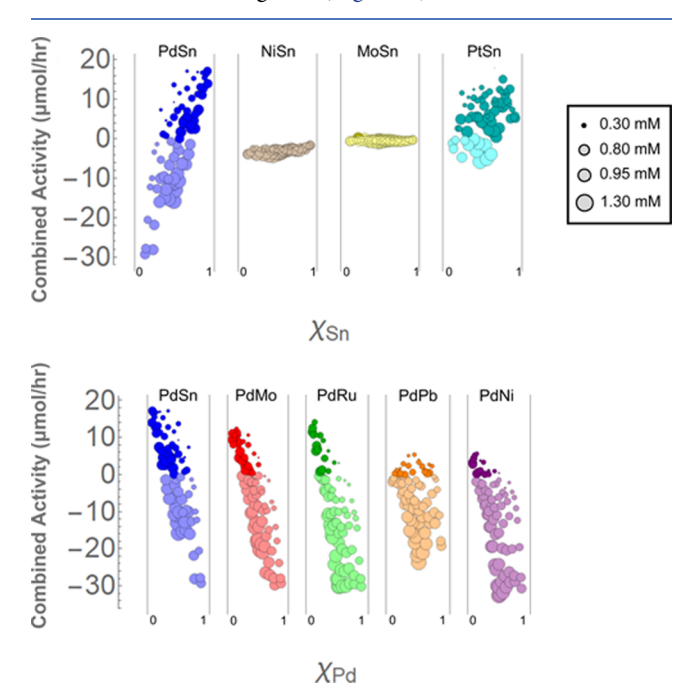


**Figure 6.** (Top) Combined activity for plates containing Sn by mole fraction of Sn in each catalyst composition. (Bottom) Combined activity for plates containing Pd by mole fraction of Pd in each catalyst composition. Darker points represent areas of synergistic activity, whereas lighter points represent antagonistic activity. Bubble size represents the added concentrations of each metal in the bimetallic combinations, according to the legend.

strate that there is generally a peak in the combined activity which supersedes the individual metal activities. This enhancement can be observed prominently with metal combinations: Pd/Sn, Pd/Mo, Pd/Ru, and Pt/Sn. Although the combined activity uncovers important insights into the synergy between the composing metals, it does not quantify the overall capacity of a bimetallic catalyst.

The two most significant findings are uncovered by the Pd/Sn and Pt/Sn experiments, which exhibit the highest maximum combined activities. As monometallic catalysts, Pd and Pt are already highly productive catalysts, and by combining them with Sn (at an optimal mole fraction), Pd and Pt were made more active. A table presenting the combined activities and metal salt concentrations associated therein can be found in the Supporting Information (Table S2). From these results, we can envision the capacity of a system to operate with substantially less Pd than was expected. Thus, of these two bimetallic systems, Pd/Sn is of greater interest because the highest combined activity was observed at 7.7% Pd, whereas the

highest synergistic effect found for Pt/Sn was observed at 33% Pt.

Given that Pd becomes less catalytically active at higher concentrations, it was considered whether the addition of Sn would allow for the resulting Pd/Sn bimetallic system to remain as effective as Pd only at higher concentrations. Plotting the maximum  $\rm H_2$  evolution rate as a function of both Pd and Sn concentration, we observe that as the Pd concentration increases in the Pd/Sn system, the maximum rate surpassed the rate of Pd only at comparable concentrations (above 0.4 mM Pd, Figures 5 and 7). Ridges and hotspots were identified following

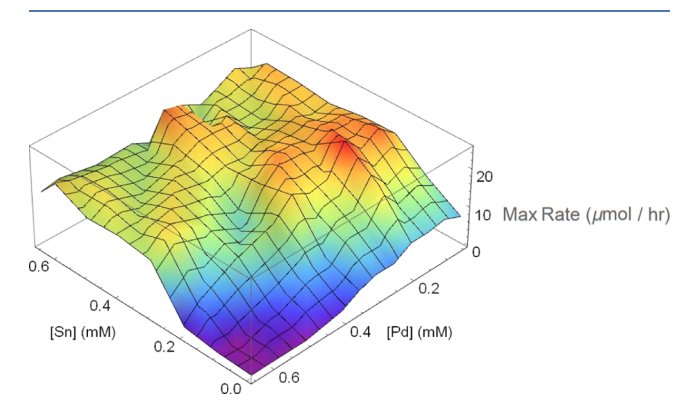
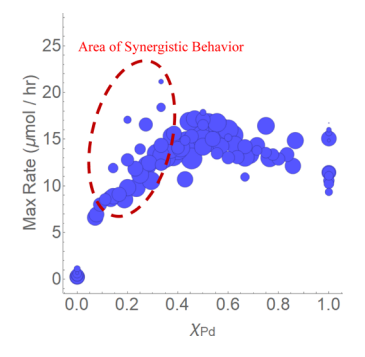


Figure 7. Maximum  $H_2$  evolution rate as measured in micromoles per hour is plotted as height against the range of concentrations tested for the Pd/Sn mixtures. Maximum rates (red peaks) are observed at 0.2 mM Pd/0.2 mM Sn and 0.3 mM Pd/0.3 mM Sn.

approximately a 1:1 ratio of Pd/Sn, and peak performance is observed at 0.2 mM of each metal. These findings led to further exploration across compositional space via the mole fraction of component metals in the catalyst. We chose to express this compositional space by the fraction of Pd because it is traditionally considered to be the more active catalytic component. At higher Pd concentration, where activity is generally low (above 0.4 mM Pd, Figure 7), addition of Sn increased the catalytic rate.

As Pd/Sn exhibits clear synergy, it was chosen for further exploration and characterization. Across compositional space, the maximum rate shows a clear fit in the form of a quadratic function which peaks at 0.5  $\chi_{Pd}$  (Figure 8). This trend suggests that the fastest catalysts are made up of approximately equal parts Pd and Sn, whereas the strongest synergistic effect is



**Figure 8.** Activity of Pd/Sn demonstrated across compositions with bubble size representing the concentration of the combined catalysts with the bimetallic mixtures of highest synergy encircled in red.

ACS Catalysis pubs.acs.org/acscatalysis Research Article

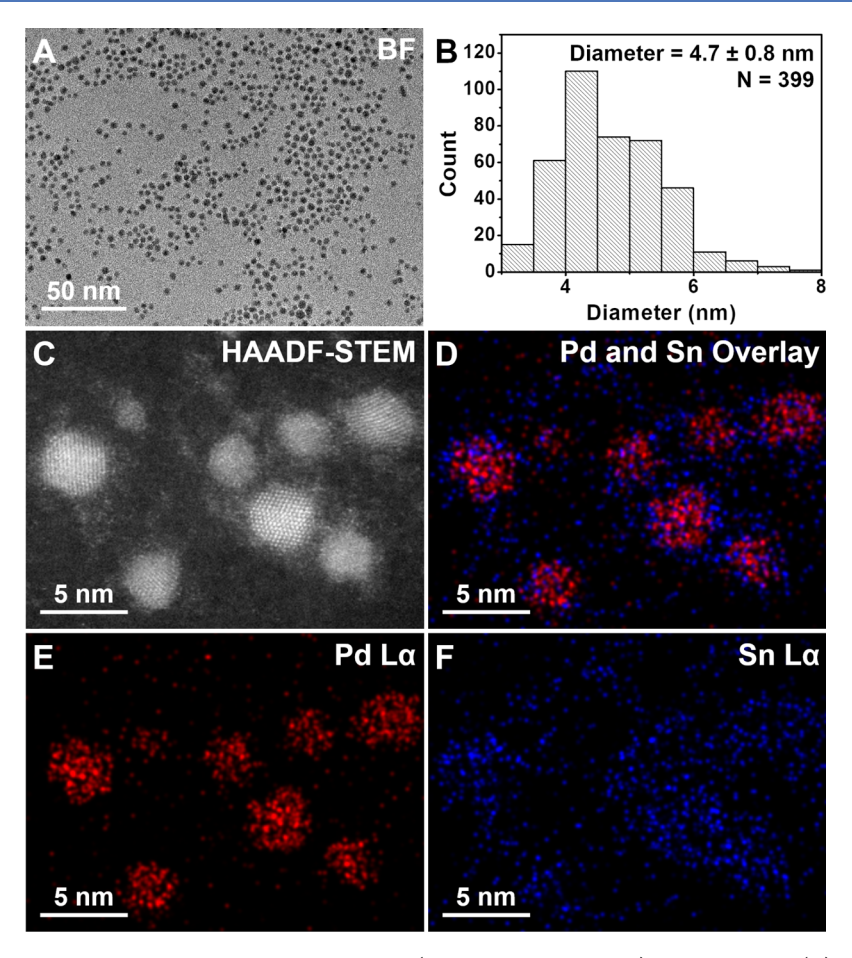


Figure 9. Characterization of the Pd/Sn system with the highest activity (0.2 mM Pd/0.2 mM Sn). Representative (A) BF TEM image and (B) size histogram. (C) HAADF–STEM image and (D–F) STEM–EDS maps, where Pd Lα signal is represented in red and Sn Lα signal is represented in blue. Corresponding linescans can be found in Figure S6.

observed in Pd/Sn with more Sn and can be seen at Pd fractions between 0.1 and 0.3 mM.

The 1:1 ratio of Pd/Sn was then considered for detailed characterization due to its substantial activity and intriguing synergy. In order to analyze the resulting Pd/Sn solution postirradiation, an unwashed aliquot was imaged using TEM, which indicated that the colloids form in situ during the reaction and that these particles are pseudospherical with an average diameter of  $4.7 \pm 0.8$  nm (Figure 9A,B). STEM-EDS was then used to determine the distribution of Pd and Sn in individual nanoparticles. The elemental maps indicate that both Pd and Sn can be found within each individual particle (Figure 9C-F, see Figure S6 for associated linescans). In addition to this most active sample (0.2 mM Pd/0.2 mM Sn), two other compositions of Pd/Sn as well as those containing only single metals (i.e., Pd only or Sn only) were also examined using TEM and STEM-EDS linescans (Figures S7 and S8). For each of these samples, particles formed in situ during the course of the water reduction reaction (Figure S7). Linescans suggest that for the other two Pd/Sn compositions, Pd and Sn can also be found within the same particle (Figure S8). In addition to the Pd- and Sncontaining samples, the other bimetallic combinations and individual metals were examined using TEM (Figure S9). XPS analyses of the single-metal compositions of interest (i.e., Pd only and Sn only) and the three Pd/Sn compositions were conducted (Figure S10 and Table S3). The Sn 3d region of the XPS spectra suggests that the 0.2 mM Sn only sample likely

contains a dominant  $\mathrm{SnO}_x$  product, whereas the Sn 3d peaks for the samples containing a mixture of Pd and Sn shift to lower binding energies, suggesting that Pd—Sn and/or Sn—Sn bonds are present. The Pd 3d region supports the mixing of Pd and Sn, where the peaks for the samples containing a mixture of Pd and Sn shift to higher binding energies as compared to the 0.2 mM Pd only sample. Taken together, these results support the mixing of Pd and Sn within the particles.

DFT data was used to determine the analogy of this volcano-like plot with known electrocatalytic volcano plots for HER activity. Much like the highly discussed volcano plots from electrochemical catalysis,  $^{9,10,32}$  we observe a peak in the middle of our compositional distribution with decreased activity as each individual metal is approached. In order to validate this claim, we used DFT calculations of metallic surfaces and machine learning-predicted surface binding energies to determine if a  $\Delta G_{\mathrm{H}^*}$  value close to 0 eV led to the experimentally determined high activity.

Previous DFT calculations and experiments showed that Pd catalysts suffer from too strong H\* binding on the surface, preventing the desorption of H\* as  $H_2$ . Therefore, weakening of H\* binding through electronic structure tuning could help improve HER catalytic activity.<sup>33</sup> To understand the experimentally observed trend in HER activity as a function of Pd/Sn ratio, we modeled various surfaces of Sn, Pd, and Pd/Sn alloys available online (Table S1)<sup>21</sup> and calculated  $\Delta G_{H^*}$  on various surfaces (Figure 10A). As our DFT calculations showed a wide

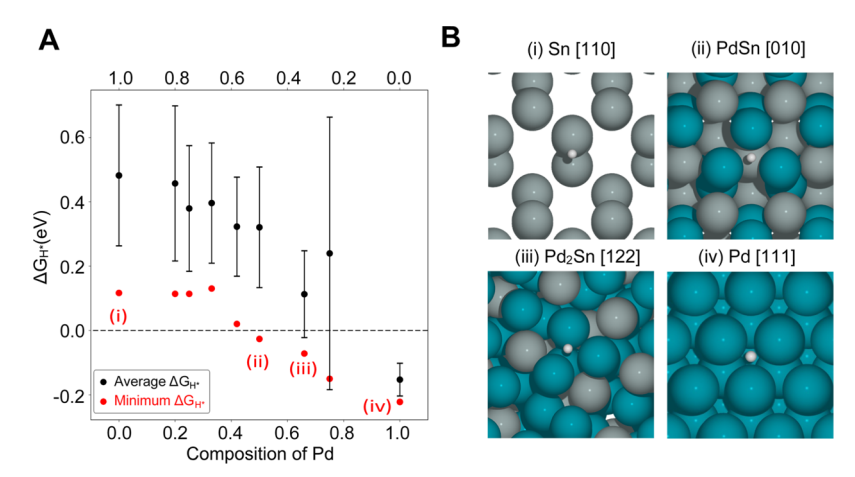
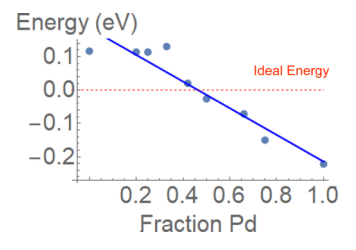


Figure 10. (A) Binding free energies of  $H^*$  on various surfaces of Sn, Pd, and Pd/Sn. Black circles with error bars indicate average binding free energies with standard deviation values for each composition. Red circles indicate the strongest binding energies. (B) Top view of the strongest binding on (i) Sn, (ii) PdSn, (iii) Pd2Sn, and (iv) Pd. Grey, turquoise, and white balls denote Sn, Pd, and H atoms, respectively.

range of binding energies on all surfaces, we plotted averages and standard deviations of  $\Delta G_{H^*}$  as well as the strongest  $\Delta G_{H^*}$ , which could represent experimentally measured catalytic activities of HER. 34 We observed a general trend that increasing the concentration of Pd  $(r_{Pd})$  strengthens the H\* binding strength. Particularly, the strongest binding energy on PdSn ( $r_{Pd}$ = 0.5) sharply dropped from  $Sn_2Pd$  ( $r_{Pd}$  = 0.33) by 0.6 eV. This drop could originate from the increased content of Pd and a generation of new Pd-Pd-Pd fcc hollow site on PdSn (Figure 10B). Further increasing  $r_{\rm Pd}$  strengthened H\* binding strength, making H\* desorption the reaction-limiting step. Thus, DFT calculations suggest that  $r_{\rm Pd}$  of ~0.5 is the optimal composition, as in the experiments and explain the improved catalytic activity. We note that  $\Delta G_{H^*}$  of Sn surfaces are mostly weak ( $\sim$ 0.5 eV) but some of them deviate from the general trend ( $\sim$ 0.1 eV). One example of the strong binding site is illustrated in Figure 10B, where H\* binds singly to the Sn atom. This strong binding could be attributed to the diamond structure of  $\alpha$ -Sn with four coordinate Sn atoms. On the other hand, Sn forms more packed structures as Sn and Pd form intermetallic alloys, and those highly active sites presented in  $\alpha$ -Sn disappear.

Using these computationally determined free energies of hydrogen adsorption and the observed catalytic activity across the tested compositional distribution of Pd and Sn could then demonstrate that the Sabatier principle allows the prediction of activity in these heterogenous photodriven catalytic systems. For each composition of Pd/Sn, the lowest binding energy was taken, and a fit function was made across the mole fraction of Pd in the particles (Figure 11). High activity is expected for our catalysts as  $\Delta G_{H^*}$  approaches 0 eV, as this is then a thermoneutral reaction. It is noteworthy that the tested Pd/Sn compositional space crosses this value, and more noteworthy that this intersection occurs around  $\chi_{Pd}$  of 0.5 where the maximum activity was experimentally observed.

The linear fit ( $R^2$  = 0.90) from Figure 11 was used to estimate the composition weighted-average adsorption energy for each Pd/Sn unique composition within the experimentally tested data set. When the composition weighted-average adsorption energy is plotted against the rate of  $H_2$  evolution (Figure 12) for the same composition, the peak activity occurs near an adsorption energy of 0 eV, similar to the maximum activity observed in HER volcano plots. This suggests that Pd/Sn bimetallic particles have formed, and that their catalytic activity



**Figure 11.** Minimum hydrogen adsorption energy calculated across a range of Pd/Sn compositions, fit with a linear regression to a correlation coefficient of 0.90. The fit function crosses the ideal energy of the top of electrocatalytic volcano plots of 0 eV indicated by the red dotted line, suggesting maximum activity would appear around 0.5 mole fraction Pd.

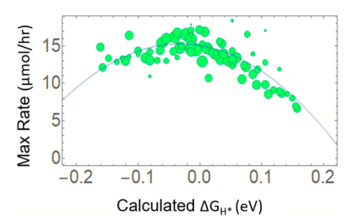


**Figure 12.** Experimentally determined activities of Pd/Sn systems plotted against the calculated minimum energy of hydrogen adsorption as determined by the fit line seen in Figure 10. Bubble size represents catalyst concentration. The parabolic fit function shown has a correlation coefficient of 0.98.

is similar to those in electrochemical HER studies. It is, of course, possible that there are other explanations for this observation, and further studies are needed to determine what those are. It also shows, however, that using this system and this computational model enables a rapid search through other metallic combinations and lays groundwork for computationally guided abbreviated searches for ideal candidates.

#### CONCLUSIONS

Through the use of our newly designed and developed 96-well parallelized photoreactor and calibrated colorimetric  $\rm H_2$  detection using DetecTape, we have been able to determine the catalytic activities of over 700 bimetallic WRCs formed in situ using chloride salts of Pd, Sn, Pt, Ru, Mo, Pb, and Ni. Of these bimetallic combinations, we observed synergistic activity,

promoting above the activity of Pt and Pd alone, in a host of candidate combinations including Pd/Mo, Pd/Ru, Pt/Sn, and Pd/Sn. We chose to further investigate Pd/Sn as its most synergistic composition occurred at a low relative fraction of the precious metal Pd (7.7% of the WRC). Exploration of the 1:1 Pd/Sn composition (0.2 mM Pd/0.2 mM Sn) revealed the in situ formation of pseudospherical nanoparticles (4.7  $\pm$  0.8 nm) in which both Pd and Sn elements were found within the same particle through the use of electron microscopy techniques. Pairing experimental data on the activity of Pd/Sn WRCs with DFT-determined energies of adsorption of hydrogen to the surface revealed that these photocatalytic systems mirror the maximum activity seen in electrocatalytic H2 evolution volcano plots. Following the Sabatier principle, it was seen that the optimum binding energy in the case of this Pd/Sn bimetallic combination was -0.036 eV, matching the theoretically predicted maximum for electrocatalysts at 0 eV. This reinforces the validity and precision of this new method of parallel H<sub>2</sub> detection and lays a framework for rapid isolation of optimized catalysts through corroboration of theoretical and experimental data on a large scale.

## ASSOCIATED CONTENT

## Supporting Information

The Supporting Information is available free of charge at https://pubs.acs.org/doi/10.1021/acscatal.9b05404.

Time resolved H<sub>2</sub> evolution plots for Pd/Sn and Ni/Sn, Pd/Pb and Pt/Sn, Pd/Mo and Pd/Ru, and Pd/Ni and Mo/Sn; fit functions for all tested single-metal WRCs; studied MPIDs and compositions; combined activity values for all tested metal combinations; linescans of 0.2 mM Pd/0.2 mM Sn; BF TEM images and size distributions for Pd, Sn, and Pd/Sn; dark-field images and linescans of Pd/Sn; BF TEM images of non-Pd/Sn systems tested; XPS data; full reaction time scale calibration; and text version of the analysis code (PDF)

Mathematica code for image analysis (.nb) and datasheet of raw results (XLSX)

## AUTHOR INFORMATION

## **Corresponding Author**

Stefan Bernhard — Department of Chemistry, Carnegie Mellon University, Pittsburgh, Pennsylvania 15213, United States; orcid.org/0000-0002-8033-1453; Email: bern@cmu.edu

#### **Authors**

Eric M. Lopato — Department of Chemistry, Carnegie Mellon University, Pittsburgh, Pennsylvania 15213, United States Emily A. Eikey — Department of Chemistry, University of Pittsburgh, Pittsburgh, Pennsylvania 15260, United States; orcid.org/0000-0001-9589-4331

Zoe C. Simon — Department of Chemistry, University of
Pittsburgh, Pittsburgh, Pennsylvania 15260, United States
Seoin Back — Department of Chemical and Biomolecular
Engineering, Sogang University, Seoul 04107, Republic of Korea
Kevin Tran — Department of Chemical Engineering, Carnegie
Mellon University, Pittsburgh, Pennsylvania 15213, United States
Jacqueline Lewis — Department of Chemistry, Carnegie Mellon
University, Pittsburgh, Pennsylvania 15213, United States
Jakub F. Kowalewski — Department of Chemistry, Carnegie
Mellon University, Pittsburgh, Pennsylvania 15213, United States

Sadegh Yazdi — Renewable and Sustainable Energy Institute, University of Colorado at Boulder, Boulder, Colorado 80309, United States; Oorcid.org/0000-0002-3470-9398

John R. Kitchin — Department of Chemical Engineering, Carnegie Mellon University, Pittsburgh, Pennsylvania 15213, United States; Occid.org/0000-0003-2625-9232

Zachary W. Ulissi — Department of Chemical Engineering, Carnegie Mellon University, Pittsburgh, Pennsylvania 15213, United States; orcid.org/0000-0002-9401-4918

Jill E. Millstone — Department of Chemistry, University of Pittsburgh, Pittsburgh, Pennsylvania 15260, United States; orcid.org/0000-0002-9499-5744

Complete contact information is available at: https://pubs.acs.org/10.1021/acscatal.9b05404

#### Notes

The authors declare no competing financial interest.

## ACKNOWLEDGMENTS

This work was supported in part by the University of Pittsburgh and Carnegie Mellon University. S.B. gratefully acknowledges National Science Foundation (NSF) funding CHE 1764353 for this work. Seed funding for the development of the highthroughput reactors came from Carnegie Mellon University's Kavcic-Moura Fund and Manufacturing Futures Initiative. E.M.L. was supported by the Steinbrenner Institute Graduate Fellowship and the ARCS Foundation Pittsburgh Chapter. Seed code used to generate the image analysis program was provided by Tomasz Kowalewski. This research used resources of the National Energy Research Scientific Computing Center (NERSC), a U.S. Department of Energy Office of Science User Facility operated under Contract no. DE-AC02-05CH11231. This research was supported by the U.S. Department of Energy, Office of Science, Office of Basic Energy Sciences, Data Science for Knowledge Discovery for Chemical and Materials Research program, under Award DE-SC0020392. E.A.E. acknowledges the NSF Graduate Research Fellowship Program under grant no. 1747452. Z.C.S. acknowledges the Dietrich School of Arts and Sciences at the University of Pittsburgh for the Arts and Sciences Graduate Fellowship. The support from the Facility for Electron Microscopy of Materials at the University of Colorado at Boulder (CU FEMM) is acknowledged.

### REFERENCES

- (1) Lewis, N. S.; Nocera, D. G. Powering the planet: Chemical challenges in solar energy utilization. *Proc. Natl. Acad. Sci. U.S.A.* **2006**, 103, 15729–15735.
- (2) (a) Staykov, A.; Lyth, S. M.; Watanabe, M. In *Hydrogen Energy Engineering*; Sasaki, K., Li, W.-H., Hayashi, A., Yamabe, J., Ogura, T., Lyth, S. M., Eds.; Springer: Japan, 2016; pp 159–174. (b) Call, A.; Franco, F.; Kandoth, N.; Fernandez, S.; Fernández, M.; Pérez-Prieto, J.; Luis, J. M.; Lloret-Fillol, J. Understanding Light-driven H<sub>2</sub> Evolution through the Electronic Tuning of Aminopyridine Cobalt Complexes. *Chem. Sci.* 2018, 9, 2609–2619. (c) Kuehnel, M. F.; Creissen, C. E.; Sahm, C. D.; Wielend, D.; Schlosser, A.; Orchard, K. L.; Reisner, E. ZnSe Nanorods as Visible-Light Adsorbers for Photocatalytic and Photoelectrochemical H<sub>2</sub> Evolution in Water. *Angew. Chem., Int. Ed.* 2019, 58, 5059–5063.
- (3) Curtin, P. N.; Tinker, L. L.; Burgess, C. M.; Cline, E. D.; Bernhard, S. Structure—Activity Correlations Among Iridium(III) Photosensitizers in a Robust Water-Reducing System. *Inorg. Chem.* **2009**, *48*, 10498–10506.

- (4) Kagalwala, H. N.; Chirdon, D. N.; Mills, I. N.; Budwal, N.; Bernhard, S. Light-Driven Hydrogen Generation from Microemulsions Using Metallosurfactant Catalysts and Oxalic Acid. *Inorg. Chem.* **2017**, *56*, 10162–10171.
- (5) Lv, H.; Xi, Z.; Chen, Z.; Guo, S.; Yu, Y.; Zhu, W.; Li, Q.; Zhang, X.; Pan, M.; Lu, G.; Mu, S.; Sun, S. A New Core/Shell NiAu/Au Nanoparticle Catalyst with Pt-like Activity for Hydrogen Evolution Reaction. J. Am. Chem. Soc. 2015, 137, 5859—5862.
- (6) Nørskov, J. K.; Bligaard, T.; Logadottir, A.; Kitchin, J. R.; Chen, J. G.; Pandelov, S.; Stimming, U. Trends in the Exchange Current for Hydrogen Evolution. *J. Electrochem. Soc.* **2005**, *152*, J23–J26.
- (7) Tachibana, Y.; Vayssieres, L.; Durrant, J. R. Artificial Photosynthesis for Solar Water-Splitting. *Nat. Photonics* **2012**, *6*, 511–518.
- (8) (a) Chen, X.; Shen, S.; Guo, L.; Mao, S. S. Semiconductor-based Photocatalytic Hydrogen Generation. *Chem. Rev.* **2010**, *110*, 6503–6570. (b) Stein, H. S.; Guevarra, D.; Newhouse, P. F.; Soedarmadji, E.; Gregoire, J. M. Machine learning of optical properties of materials predicting spectra from images and images form spectra. *Chem. Sci.* **2019**, *10*, 47–55.
- (9) Greely, J.; Mavrikakis, M. Surface and Subsurface Hydrogen: Adsorption Properties on Transition Metals and Near-Surface Alloys. *J. Phys. Chem. B* **2005**, *109*, 3460–3471.
- (10) Greeley, J.; Nørskov, J. K.; Kibler, L. A.; El-Aziz, A. M.; Kolb, D. M. Hydrogen Evolution Over Bimetallic Systems: Understanding the Trends. *ChemPhysChem* **2006**, *7*, 1032–1035.
- (11) (a) Laursen, A. B.; Varela, A. S.; Dionigi, F.; Fanchiu, H.; Miller, C.; Trinhammer, O. L.; Rossmeisl, J.; Dahl, S. Electrochemical Hydrogen Evolution: Sabatier's Principle and the Volcano Plot. J. Chem. Educ. 2012, 89, 1595–1599. (b) Jaramillo, T. F.; Jørgensen, K. P.; Bonde, J.; Nielsen, J. H.; Horch, S.; Chorkendorff, I. Identification of Active Edge Sites for Electrochemical H<sub>2</sub> Evolution from MoS<sub>2</sub> Nanocatalysts. Science 2007, 317, 100–102. (c) Sheng, W.; Myint, M.; Chen, J. G.; Yan, Y. Correlating the Hydrogen Evolution Reaction Activity in Alkaline Electrolytes with the Hydrogen Binding Energy on Monometallic Surfaces. Energy Environ. Sci. 2013, 6, 1509–1512. (d) Zheng, Y.; Jiao, Y.; Jaroniec, M.; Qiao, S. Z. Advancing the Electrochemistry of the Hydrogen-Evolution Reaction through Combining Experiment and Theory. Angew. Chem., Int. Ed. 2015, 127, 52–66.
- (12) (a) Shimazu, K.; Goto, R.; Tada, K. Electrochemical Reduction of Nitrate Ions on Tin-Modified Platinum and Palladium Electrodes. *Chem. Lett.* **2002**, *31*, 204–205. (b) Birdja, Y. Y.; Yang, J.; Koper, M. T. M. Electrocatalytic Reduction of Nitrate on Tin-Modified Palladium Electrodes. *Electrochim. Acta* **2014**, *140*, 518–524. (c) Roveda, A.; Benedetti, A.; Pinna, F.; Strukul, G. Palladium-tin Catalysts on Acrylic Resins for the Selective Hydrogenation of Nitrate. *Inorg. Chim. Acta* **2003**, *349*, 203–208. (d) Tada, K.; Kawaguchi, T.; Shimazu, K. High Electrocatalytic Performance of Pd/Sn/Au Electrodes for Nitrate Reduction. *J. Electroanal. Chem.* **2004**, *572*, 93–99.
- (13) (a) Barbosa, D. P.; Tchiéta, P.; Rangel, M. d. C.; Epron, F. The Use of a Cation Exchange Resin for Palladium-Tin and Palladium-Indium Catalysts for Nitrate Removal in Water. *J. Mol. Catal. A: Chem.* **2013**, *366*, 294–302. (b) Berndt, H.; Mönnich, I.; Lücke, B.; Menzel, M. Tin Promoted Palladium Catalysts for Nitrate Removal From Drinking Water. *Appl. Catal., B* **2001**, *30*, 111–122.
- (14) Freakley, S. J.; He, Q.; Harrhy, J. H.; Lu, L.; Crole, D. A.; Morgan, D. J.; Ntainjua, E. N.; Edwards, J. K.; Carley, A. F.; Borisevich, A. Y.; Kiely, C. J.; Hutchings, G. J. Palladium-Tin Catalysts for the Direct Synthesis of H<sub>2</sub>O<sub>2</sub> with High Selectivity. *Science* **2016**, *351*, 965–968.
- (15) Bond, G. C.; Molloy, L. R.; Fuller, M. J. Oxidation of Carbon Monoxide over Palladium-Tin(IV) Oxide Catalysts: An Example of Spillover Catalysis. *J. Chem. Soc., Chem. Commun.* **1975**, 829, 796–797.
- (16) Du, W.; Mackenzie, K. E.; Milano, D. F.; Deskins, N. A.; Su, D.; Teng, X. Palladium-Tin Alloyed Catalysts for the Ethanol Oxidation Reaction in an Alkaline Medium. ACS Catal. 2012, 2, 287–297.
- (17) Tinker, L. L.; Mcdaniel, N. D.; Curtin, P. N.; Smith, C. K.; Ireland, M. J.; Bernhard, S. Visible Light Induced Catalytic Water Reduction without an Electron Relay. *Chem. Eur. J.* **2007**, *13*, 8726–8732.

- (18) (a) Kresse, G.; Hafner, J. Ab Initio Molecular Dynamics for Open-Shell Transition Metals. *Phys. Rev. B: Condens. Matter Mater. Phys.* **1993**, *48*, 13115–13118. (b) Kresse, G.; Furthmüller, J. Efficiency of ab-initio Total Energy Calculations for Metals and Semiconductors Using a Plane-Wave Basis Set. *Comput. Mater. Sci.* **1996**, *6*, 15–50.
- (19) Hammer, B.; Hansen, L. B.; Nørskov, J. K. Improved Adsorption Energetics within Density-Functional Theory Using Revised Perdew-Burke-Ernzerhof Functionals. *Phys. Rev. B: Condens. Matter Mater. Phys.* 1999, 59, 7413–7421.
- (20) Kresse, G.; Joubert, D. From Ultrasoft Pseudopotentials to the Projector Augmented-Wave Method. *Phys. Rev. B: Condens. Matter Mater. Phys.* **1999**, *59*, 1758–1775.
- (21) Jain, A.; Ong, S. P.; Hautier, G.; Chen, W.; Richards, W. D.; Dacek, S.; Cholia, S.; Gunter, D.; Skinner, D.; Ceder, G.; Persson, K. A. Commentary: The Materials Project: A Materials Genome Approach to Accelerating Materials Innovation. *APL Mater.* **2013**, *1*, 011002.
- (22) Tran, K.; Ulissi, Z. W. Active Learning Across Intermetallics to Guide Discovery of Electrocatalysts for CO<sub>2</sub> Reduction and H<sub>2</sub> Evolution. *Nat. Catal.* **2018**, *1*, 696–703.
- (23) Larsen, A. H.; Mortensen, J. J.; Blomqvist, J.; Castelli, I. E.; Christensen, R.; Dulak, M.; Friis, J.; Groves, M. N.; Hammer, B.; Hargus, C.; Hermes, E. D.; Jennings, P. C.; Jensen, P. B.; Kermode, J.; Kitchin, J. R.; Kolsbjerg, E. L.; Kubal, J.; Kaasbjerg, K.; Lysgaard, S.; Maronsson, J. B.; Maxson, T.; Olsen, T.; Pastewka, L.; Peterson, A.; Rostgaard, C.; Schiotz, J.; Schutt, O.; Strange, M.; Thygesen, K. S.; Begge, T.; Vilhelmsen, L.; Walter, M.; Zeng, Z.; Jacobsen, K. W. The Atomic Simulation Environment a Python Library for Working with Atoms. J. Phys. Condens. Matter 2017, 29, 273002.
- (24) Skúlason, E.; Tripkovic, V.; Björketun, M. E.; Gudmundsdóttir, S.; Karlberg, G.; Rossmeisl, J.; Bligaard, T.; Jónsson, H.; Nørskov, J. K. Modeling the Electrochemical Hydrogen Oxidation and Evolution Reactions on the Basis of Density Functional Theory Calculations. *J. Phys. Chem. C* **2010**, *114*, 18182–18197.
- (25) Kirch, M.; Lehn, J.-M.; Sauvage, J.-P. Hydrogen Generation by Visible Light Irradiation of Aqueous Solutions of Metal Complexes. An Approach to the Photochemical Conversion and Storage of Solar Energy. *Helv. Chim. Acta* **1979**, *62*, 1345–1384.
- (26) Mills, I. N.; Porras, J. A.; Bernhard, S. Judicious Design of Cationic Cyclometalated Ir(III) Complexes for Photochemical Energy Conversion and Optoelectronics. *Acc. Chem. Res.* **2018**, *51*, 352–364.
- (27) Cline, E. D.; Bernhard, S. The Transformation and Storage of Solar Energy: Progress Towards Visible-Light Induced Water Splitting. *CHIMIA Int. J. Chem.* **2009**, *63*, 709–713.
- (28) Terki, R.; Simoneau, L.-P.; Rochefort, A. Tailoring the Photoluminescence Properties of Ionic Iridium Complexes. *J. Phys. Chem. A* **2009**, *113*, 534–541.
- (29) Cline, E. D. Orchestrating Electron Transfer for Solar Energy Conversion: Homogeneous Catalytic Systems and Supramolecular Assemblies, Ph.D. Dissertation, Princeton University, Princeton, NJ, 2010.
- (30) Curtin, P. N.; Tinker, L. L.; Burgess, C. M.; Cline, E. D.; Bernhard, S. Structure-Activity Correlations Among Iridium(III) Photosensitizers in a Robust Water-Reducing System. *Inorg. Chem.* **2009**, *48*, 10498–10506.
- (31) Nash, A.; Nash, P. The Ni-Pd (Nickel-Palladium) System. *Bull. Alloy Phase Diagrams* **1984**, *5*, 446–450.
- (32) Greeley, J.; Jaramillo, T. F.; Bonde, J.; Chorkendorff, I.; Nørskov, J. K. Computational High-Throughput Screening of Electrocatalytic Materials for Hydrogen Evolution. *Nat. Mater.* **2006**, *5*, 909–913.
- (33) Shao, M. Palladium-based Electrocatalysts for Hydrogen Oxidation and Oxygen Reduction Reactions. *J. Power Sources* **2011**, 196, 2433–2444.
- (34) Benck, J. D.; Hellstern, T. R.; Kibsgaard, J.; Chakthranont, P.; Jaramillo, T. F. Catalyzing the Hydrogen Evolution Reaction (HER) with Molybdenum Sulfide Nanomaterials. *ACS Catal.* **2014**, *4*, 3957–3971.